Microstructure evolution under [110] creep in Ni-base superalloys

M Cottura, Benoît Appolaire, A Finel, Y Le Bouar

HAL Id: hal-03815197
https://hal.science/hal-03815197v2

Submitted on 14 Oct 2022

Microstructure evolution under [110] creep in Ni-based superalloys

M. Cottura[1,2], B. Appolaire[1], A. Finel[2], Y. Le Bouar[2]

[1] *Université de Lorraine, CNRS, IJL, Nancy F–54000, France*

[2] *Laboratoire d'Etude des Microstructures, ONERA, CNRS, Université Paris-Saclay, 92320 Châtillon, France*

Abstract

Microstructure evolutions in Ni-based superalloys are investigated during [110] creep loading using 3D and 2D phase field simulations. A recently developed phase field model coupled to a crystal plasticity model based on dislocation densities is employed. The model uses a storage-recovery law for the dislocation density of each glide system and a hardening matrix to account for the short-range interactions between dislocations. We show that small misorientations of the tensile axis strongly modify the evolution: rafting is observed for small deviations, as opposed to a microstructure made of rod-like precipitates when loading is performed along a perfectly aligned [110] direction. Depending on the precise direction of the mechanical load, different evolutions are obtained accompanied by strong modification of the macroscopic creep behavior, explaining the variety of results observed experimentally. The relative role of inhomogeneous and anisotropic elastic and plastic driving forces is also investigated, plasticity being the main driving force for rafting in the considered case. In addition, our calculations show that the initial dislocation density slightly modifies the precipitates morphology but the creep curve is significantly impacted.

Keywords: phase transformation, crystal plasticity, phase field modeling, superalloys

1. Introduction

Ni-based superalloys are widely used for aeronautical and industrial gas turbine applications due to their excellent mechanical behavior at high temperatures. They owe this behavior to their microstructure consisting of a high volume fraction of strengthening γ' cuboidal precipitates (L1$_2$ ordered structure) embedded in a γ matrix (face-centered cubic solid solution). During service, directional coarsening (rafting) of γ' precipitates occurs, with a strong dependance on temperature and creep loading. Due to its technological importance, rafting has been extensively investigated during the last decades. Rafting has also been the focus of more fundamental studies as Ni-based superalloys appear to be a relevant candidate for investigating strong couplings between diffusion-controlled phase transformations, elasticity and plasticity.

Most experimental studies have focused on the creep properties of [100]-oriented single crystals because the [100] direction is the principal stress direction in monocrystalline turbine blades [2–4]. There is a good comprehension of the different factors influencing rafting under [100] creep, such as the role of the elastic inhomogeneity between the γ and γ' phase, the lattice mismatch, the applied stress and/or the plastic activity. However, in the root and shroud section of the blade or in some highly cooled complex blades, stresses may be significant in other orientations [5]. Therefore, it is necessary to investigate microstructure evolution and its associated mechanical behavior under more complex creep conditions.

---

*Corresponding author: yann.lebouar@onera.fr

Several experimental studies have been carried out about superalloys under [110] creep loading [2, 6–18] but a number of points needs to be further addressed. First, there is a disparity of results regarding the observed microstructures. Kuttner et al. [6] reported that, for a SRR99 superalloy under [011] tensile creep, the cubic morphology is maintained at 1033 K whereas a rod morphology perpendicular to the applied load is observed at 1173 K, in agreement with Tien and Copley for the Udimet-700 [3]. Tian et al. [11, 12] investigated [110] tensile creep under high-temperature and low-stress creep conditions reporting rafting 45° away from the loading direction. In the case of the LEK 94 superalloy at 1293 K, a microstructure also made of rafts is observed but in two 45° directions in Agudo Jacome et al. [13]. Tian et al. [11, 12] hypothesized that their microstructure was the result of a small misorientation of the specimen (4°) from the [011] orientation. In addition, rafting appears to be a microstructural evolution quite sensitive to small microstructural differences [13, 14]. More recently, [011]-oriented samples of first-generation Ni-based single-crystal superalloys was investigated both experimentally and numerically. Using 3D volume reconstruction of SEM microscopy imaging, the cuboidal microstructure was shown to first elongate along the cubic axis perpendicular to the tensile axis, then form platelets by coalescence along the two other cubic directions [26]. However, complete rafting was not obtained in the 3D phase field simulations realized in the study. A second point that need to be addressed is the associated mechanical behavior resulting from the different microstructures observed and how they will affect the creep behavior of the material.

This paper aims at understanding the morphological transformation path of the γ/γ' microstructure during [110] creep loading, together with its mechanical properties, using phase field modeling. To improve our understanding, the influence of a small crystallographic deviation from the [110] direction, as well as the respective role of the elastic and plastic driving forces during this evolution, is investigated. The phase field method has emerged as a powerful method for tackling microstructure evolutions during phase transformations, especially when elastic coherency stresses are generated, enabling the simulation of complex evolution problems such as the formation of chessboard-like structures in decomposing Co-Pt alloys [19], the formation of complex multi-domain pattern during coherent hexagonal to orthorhombic transformation [20], the formation of complex laminates during displacive transitions [21] and the evolution of bimodal microstructures in polycrystalline superalloys [22]. In the context of rafting in Ni-based superalloys, a few works have naturally extended the phase field model to include isotropic plasticity [23] and anisotropic plasticity, either approximately [24] or relying on a more complete and well tested crystal plasticity framework [25, 26]. In this work, we have employed a recent modeling framework [27] in which a classical phase field model for the description of the phase transformation is coupled with a crystal plasticity model based on dislocation densities.

The paper is structured as follows. First, the phase field model and the dislocation density based crystal plasticity model, as well as their coupling, will be briefly described in §2. Data and input parameters specific to Ni-based superalloys will be carefully defined and specified with respect to available experiments. Next, the evolution of the two-phase microstructure under [110] creep load is analyzed in Section §3, first using 3D simulations (§3.1), followed by a 2D systematic study (§3.2).

2. Model

In this work, the Phase Field method has been used for its ability to handle easily morphological evolutions at the mesoscale and its ability to couple many phenomena. The main ingredients of the phase field model are briefly presented in this section. Further details can be found in Ref. [27].

2.1. Phase Field Model

At equilibrium, Ni-based superalloys feature both the disordered γ and ordered γ' phases. Following [25, 28, 29], the microstructure is characterized by a concentration field c($\underline{r}$,t) and three long-range order parameter fields $\eta_{i=1,3}(\underline{r}, t)$. Indeed, the four translational variants of γ' are described by the following long-range order parameters: $\{\eta_1, \eta_2, \eta_3\} = \eta_0\{1, 1, 1\}, \eta_0\{\bar{1}, \bar{1}, 1\}, \eta_0\{\bar{1}, 1, \bar{1}\}, \eta_0\{1, \bar{1}, \bar{1}\}$. As the main ingredient of

phase field models, the mesoscopic free energy functional F is taken as the sum of a chemical F_{ch} and an elastic F_{el} contributions.

The evolution of the fields are governed by the following kinetic equations:

$$\frac{\partial c}{\partial t}(\underline{r},t) = M\nabla^2 \frac{\delta F}{\delta c(\underline{r},t)} \tag{1}$$

$$\frac{\partial \eta_i}{\partial t}(\underline{r},t) = -L \frac{\delta F}{\delta \eta_i(\underline{r},t)} \tag{2}$$

where the kinetic coefficients M and L, related to diffusion and structural relaxation respectively, are assumed constant.

In addition, static mechanical equilibrium can be safely assumed in diffusive phase transformations. It is numerically solved at each time step using a fixed-point algorithm [29].

2.1.1. Ginzburg-Landau free energy

The chemical free energy accounts for the volume free energy associated with phase transformation and interface energies. This free energy is given by a standard Ginzburg-Landau functional:

$$F_{ch}(c,\{\eta_i\}) = \int f_{hom}(c,\{\eta_i\}) + \frac{\lambda}{2}|\nabla c|^2 + \frac{\beta}{2}\sum_i |\nabla \eta_i|^2 \ d^3r \tag{3}$$

where $f_{hom}(c,\{\eta_i\})$ is the free energy density of an homogeneous system characterized by the concentration c and order parameters η_i. The coefficients λ and β of the gradient terms, related to the energies of γ/γ' interfaces and γ'/γ' anti-phase boundaries, have been prescribed constant values. The free energy density of an homogeneous system $f_{hom}(c,\eta_i)$ is approximated by a Landau polynomial expansion with respect to the order parameters as defined in [29].

2.1.2. Elastic energy

In the framework of linear elasticity, the potential elastic energy reads:

$$F_{el}(\underset{\sim}{\varepsilon}^{el}) = -V\underset{\sim}{\sigma}^a : \bar{\varepsilon} + \frac{1}{2}\int_V \underset{\sim}{\varepsilon}^{el} : \underset{\approx}{\lambda} : \underset{\sim}{\varepsilon}^{el} \ d^3r \tag{4}$$

where $\underset{\approx}{\lambda}$, $\underset{\sim}{\varepsilon}^{el}$ and $\underset{\sim}{\sigma}^a$ are the elastic moduli, elastic strain and applied stress tensors, respectively. To account for inhomogeneous elasticity, $\underset{\approx}{\lambda}$ is assumed to depend linearly on $c(\underline{r})$ [29]. $\underset{\sim}{\varepsilon}(\underline{r})$ is additively decomposed into the elastic strain, the isotropic stress-free strain following Vegard's law, and the plastic strain as follows

$$\underset{\sim}{\varepsilon}(\underline{r}) = \underset{\sim}{\varepsilon}^{el}(\underline{r}) + \underset{\sim}{\varepsilon}^{0}(\underline{r}) + \underset{\sim}{\varepsilon}^{p}(\underline{r}) \tag{5}$$

2.2. Mesoscopic Dislocation Density-based Crystal Plasticity Model (MPM)

2.2.1. Plastic strain

In fcc crystals, dislocations mainly glide in 12 favorable (octahedral) slip systems defined by the normal to the glide plane $\underline{n}^\alpha$ and the slip direction $\underline{m}^\alpha$. In the small deformation framework, the plastic strain $\underset{\sim}{\varepsilon}^p$ is the sum of the crystallographic slips γ^α in each slip system α, such that:

$$\underset{\sim}{\varepsilon}^p = \sum_\alpha \gamma^\alpha \underset{\sim}{P}^\alpha \tag{6}$$

where $\underset{\sim}{P}^\alpha$ is the symmetric Schmid tensor defined by $\underset{\sim}{P}^\alpha = \frac{1}{2}(\underline{m}^\alpha \otimes \underline{n}^\alpha + \underline{n}^\alpha \otimes \underline{m}^\alpha)$ ($\otimes$ representing the dyadic product).

2.2.2. Resolved shear stresses

Glide of dislocations belonging to the system α is driven by the resolved shear stress $\tau^\alpha = \underset{\sim}{\sigma} : \underset{\sim}{P}^\alpha$ where $\underset{\sim}{\sigma}$ is the stress tensor. More precisely, dislocations will glide only if the resolved stress exceeds a certain threshold, the critical stress τ_c^α, which is expressed using a generalized Taylor formula which accounts for the interactions between slip systems in fcc crystals [30]:

$$\tau_c^\alpha = \mu b \sqrt{\sum_\beta a^{\alpha\beta} \rho^\beta} \tag{7}$$

with b the norm of the Burgers vector, μ an average shear modulus and ρ^β the total dislocation density on the slip system β. $a^{\alpha\beta}$ is the hardening matrix with $\sqrt{a^{\alpha\beta}}$ the average strength of the interaction between slip systems α and β. For the hardening matrix coefficients, we have employed the values for fcc crystals inferred in [31] from dislocation dynamics simulations.

2.2.3. Storage and recovery law

The evolution of the dislocation density is given by a standard storage-recovery balance equation following Teodosiu et al. [32]:

$$\dot{\rho}^\alpha = \frac{1}{b} \left(\frac{1}{L^\alpha} - 2\, y_c\, \rho^\alpha \right) |\dot{\gamma}^\alpha| \tag{8}$$

where L^α is the dislocation mean free path on slip system α and y_c is a characteristic length associated with the annihilation process. L^α depends on the density of obstacles encountered by dislocations, i.e. on the density of dislocations belonging to other slip systems. Following Kubin et al. [33], L^α is assumed to be inversely proportional to the critical stress:

$$L^\alpha = K / \sqrt{\sum_\beta a^{\alpha\beta} \rho^\beta} \tag{9}$$

where K is a material parameter.

2.2.4. Plastic flow rule

The dislocation density evolution is described with a phenomenological viscoplastic power law relating the plastic slip rates $\dot{\gamma}^\alpha$ to the resolved shear stress τ^α, the backstress τ_b^α and the slip hardening τ_c^α given by [34]:

$$\dot{\gamma}^\alpha = \dot{\gamma}_0 \left(\frac{|\tau^\alpha - \tau_b^\alpha|}{\tau_c^\alpha} \right)^{\frac{1}{m}} \exp\left(-\frac{\Delta G^\alpha}{k_B\, T} \right) \operatorname{sign}(\tau^\alpha - \tau_b^\alpha) \tag{10}$$

where $\dot{\gamma}_0$ and m are the reference plastic shear rate and rate sensitivity exponent, respectively. T is the absolute temperature and k_B Boltzmann's constant. The resistance to slip in system α is reproduced by the critical resolved shear stress τ_c^α, as well as by some back stress τ_b^α to account for a size dependency of plastic flow discussed hereafter. The exponential term corresponds to the thermally-activated dislocation motions where ΔG^α is the activation energy as defined in [27].

2.2.5. Back-stress

Back-stress can be incorporated into continuous formulations of plasticity. These terms, as well as the local critical stress, are reminiscent of the short-range dislocation-dislocation correlations that are not resolved at the scale at which the continuous model is elaborated [35–37]. In other words, the back and critical stresses τ_b^α and τ_c^α should emerge from the coarse graining procedure that is needed to make a link between the microscopic and mesoscopic scales. Such a procedure has already been elaborated in the simplest situation where a single two-dimensional glide system is considered [37]. However, this coarse graining procedure has still not been performed in the general situation where multiple three dimensional glide systems are

D (m^2.s^{-1})	3×10^{-19}	
σ_{exp} (mJ.m^{-2})	2	[22, 43]
δ	-0.1 (%)	[44, 45]
C_{11}^{γ} (GPa)	197	
C_{12}^{γ} (GPa)	144	
C_{44}^{γ} (GPa)	90	
$C_{11}^{\gamma'}$ (GPa)	193	
$C_{12}^{\gamma'}$ (GPa)	118	
$C_{44}^{\gamma'}$ (GPa)	124	

Table 1: Physical parameters for AM1 superalloys at $T = 950°$C.

simultaneously active. Therefore, following Ref. [27, 38], we use for the present work the following back-stress expression:

$$\tau_b^{\alpha} \;=\; -\,\frac{\mu R^2}{8}\left[\,\frac{1}{1-\nu}\,(\,\underline{\boldsymbol{m}}^{\,\alpha} \otimes \underline{\boldsymbol{m}}^{\,\alpha}\,) : (\,\nabla \otimes \nabla\gamma^{\alpha}\,) + 2\sum_{\beta}\left(\sum_{i}\delta_s^{\alpha i}\,\delta_s^{\beta i}\,\underline{\boldsymbol{p}}^{\,\beta} \otimes \underline{\boldsymbol{p}}^{\,\alpha}\right) : \left(\,\nabla \otimes \nabla\gamma^{\beta}\,\right)\right]$$

with

$$\delta_s^{\alpha i} \;=\; \left\{ \begin{array}{ll} 1 & \text{for } (\alpha\ i) = (4,13),\ (6,18),\ (8,17),\ (9,15),\ (10,16),\ (11,14) \\ & \qquad\quad (1,16),\ (2,17),\ (3,18),\ (5,14),\ (7,13),\ (12,15) \\ 0 & \text{otherwise} \end{array} \right. \tag{11}$$

where ν is an average Poisson coefficient (such as for μ in §2.3.2) and $\underline{\boldsymbol{p}}^{\,\alpha} \;=\; \underline{\boldsymbol{m}}^{\,\alpha} \times \underline{\boldsymbol{n}}^{\,\alpha}$. Edge dislocations are then parallel to $\underline{\boldsymbol{p}}$ and screw to $\underline{\boldsymbol{m}} = \underline{\boldsymbol{b}}/b$. In the spirit of Ref. [38], the length scale R should be of the same order as the discretisation scale d used in the implementation of the model. Consequently, we have chosen $R = 1.5d$.

2.2.6. Coupling PFM & MPM

The MPM is coupled to the PFM presented in §2.1 through the expression of the total strain field (Eq. (5)). $\underline{\varepsilon}^p(\underline{\boldsymbol{r}})$ evolves according to Eqs. (6) and (10). In the ranges of temperature and stress considered, only γ undergoes plastic strain while γ' behaves elastically. To reproduce this behavior, all viscoplastic parameters have been set at their values in the γ phase and the governing equations ρ^{α} and γ^{α} are only activated inside γ [27].

2.3. Input parameters

2.3.1. Physical properties and phase field parameters

The physical properties and elastic constants used in the subsequent calculations are reported in Table 1. The inhomogeneous and anisotropic elastic constants have been retrieved from [46], where it has been shown that a large inhomogeneity of the shear modulus $C' = (C_{11} - C_{12})/2$ is required to generate well-aligned cuboidal precipitates with aspect ratios close to the experimental observations of the AM1 superalloy.

Following [25], M is such as to recover the interdiffusion coefficient in γ: $D = D_0 \exp(-\Delta U/k_B T)$ with $D_0 = 1.45\ 10^{-4}$ m^{2}s^{-1} and $\Delta U = 2.8$ eV [47]. We have used $L = 100\ Md^{-2}$, where d is the grid spacing, to ensure that the overall microstructure evolution is controlled by bulk diffusion, which requires that the local relaxation of the order parameter is fast enough. We have used the equilibrium concentrations $c_{\gamma}^0 = 0.15$ and $c_{\gamma'}^0 = 0.231$ identified on the Ni-Al phase diagram at 950°C and set $c_2 = 0.18$. The procedure to select the gradient coefficients λ and β is detailed in [27].

2.3.2. Viscoplastic parameters

The coefficients of the hardening matrix $a_{\alpha\beta}$ for superalloys are given in reference [31]. In Eqs. (7) and (11), the shear modulus μ has been taken equal to $\sqrt{C'C_{44}}$ where C_{44} and C' are the two shear moduli of the γ phase. The viscoplastic parameters presented in Table 2 are identified on the macroscopic mechanical behavior of the bulk γ phase using the experimental data of Espié et al. [48] as described in Cottura et al. [27].

b (nm)	y_c (nm)	K	μ (GPa)	ν	$\dot{\gamma}_0$ (s^{-1})	m
0.256	1.6	80	48	0.31	0.001	0.04

Table 2: Viscoplastic parameters of the γ phase in the Ni-based superalloys.

3. Evolving two-phase microstructures

3.1. 3D rafting of Ni-based superalloys during creep

In this part, we present 3D simulation results of microstructure formation and evolution in Ni-based superalloys. Our goal is to investigate the widespread experimental observations on microstructure evolution and mechanical behavior in Ni-based superalloys during [110] tensile creep loading described in §1. First, we will test whether our elasto-viscoplastic phase field model is able to capture the main trends under such load using 3D simulations. A more quantitative analysis will be performed in the following section using 2D simulations (§3.2).

3.1.1. 3D cuboidal microstructure

Using the phase field model presented in Section 2, we first perform a purely elastic 3D simulation in stress-free conditions to obtain a cuboidal microstructure. The model parameters, representative of a Ni-based superalloy [27], are listed in Table 1. The simulation box size is 3.4^3 µm^3, discretized with 512^3 nodes ($d = 6.7$ nm) with periodic boundary conditions. It has been shown that such discretisation is sufficient to correctly describe microstructure evolution [59, 46].

The microstructure obtained at $T = 950°$C after $t = 9$ h is presented in Fig. 1-a. The microstructure consists of γ' cuboidal precipitates (white regions) aligned along cubic directions and separated by well-defined γ channels (dark regions). The volume fraction of the γ' precipitates is $f_v = 0.54$ and their average size is 395 nm. Note the presence of some larger areas of γ matrix phase also observed experimentally.

The autocorrelation function and Fourier transforms are often used to characterize the periodicity and anisotropy of experimental images [39]. In particular, it has been used to quantitatively analyse 2D Scanning Electron Microscopy images of Nickel-based superalloys [40, 41]. These quantities can also be computed in 3D to analyse the microstructures predicted by phase field models.

In the present work, we have calculated the spatial autocorrelation function defined as follows:

$$I(\mathbf{r}) = \left(\langle s(\mathbf{r}+\mathbf{u})\,s(\mathbf{u})\rangle - \langle s\rangle^2\right) / \left(\langle 1 - \langle s\rangle^2\rangle\right) \tag{12}$$

where brackets denote the spatial average over the simulation box

$$\langle f\rangle = \frac{1}{V}\int_V f(\mathbf{u})d^3u \tag{13}$$

and where $s(\mathbf{r})$ is an indicator function equal to -1 in the matrix and $+1$ in the precipitate. A given point belongs to a precipitate if the local concentration exceeds the threshold value $c^* = (c_\gamma^0 + c_{\gamma'}^0)/2$. Even if it
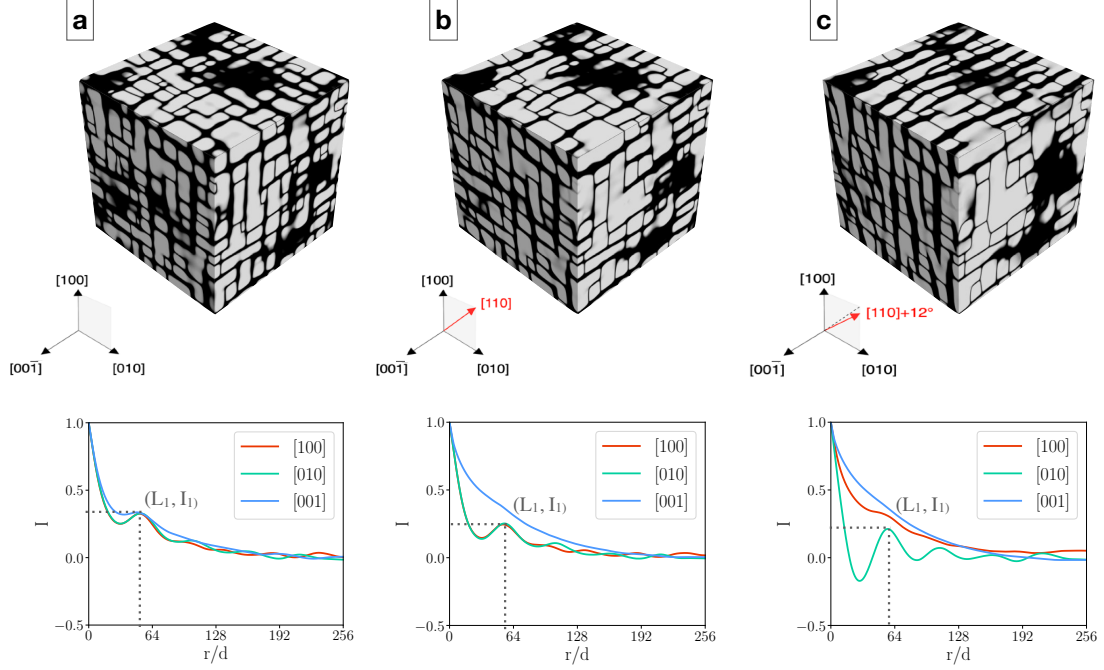
Figure 1: Top: concentration field of a - the initial cuboidal microstructure and the microstructure obtained with the full elasto-viscoplastic model after $t = 25.5$ min under b - [110] and c - [110]+12° tensile creep loading. Bottom: corresponding autocorrelation functions along the cubic axes.

is not required to compute the auto-correlation function, a threshold has been applied to the concentration field to remove the signal due to the diffusive character of the interfaces.

The autocorrelation function $I(\mathbf{r})$ computed along the cubic directions is presented in Fig. 1-a for the cuboidal microstructure. As expected, the value starts from 1 (perfect correlation) at $\mathbf{r} = 0$ and decreases to 0 (no correlation) when $|\mathbf{r}|$ is large enough.

The inverse L_2 of the initial slope of the autocorrelation function $I(\mathbf{r})$ is a characteristic length of the microstructure. For the case of an idealized microstructure consisting of identical γ' precipitates with the shape of a cuboid, it can be shown that this length is equal to $(1 - f_v)a$ where f_v is the volume fraction of precipitates and a is the size of the cuboid along the considered cubic direction. L_2 is therefore a relevant indicator for the description of the evolution of the precipitate size along a given cubic direction. In the initial microstructure, $L_2^{[100]}$, $L_2^{[010]}$ and $L_2^{[001]}$ are equal to $L^0 = (L_2^{[100]} + L_2^{[010]} + L_2^{[001]})/3 = 21d$.

In addition, the presence of a local maximum I_1, with a value close to 0.33, can be seen for all curves at about $L_1 = 51d$ revealing an imperfect periodicity of the microstructure in all three cubic directions for the distance L_1.

3.1.2. 3D microstructure evolution under tensile loading

Next, we investigate the γ/γ' microstructure evolution under [110] tensile creep load as well as the influence of a misorientation of the crystal lattice away from the perfect [110] orientation. In the rest of the paper, we will use the following notation: [110]-θ and [110]+θ indicate a load along [110] with a misorientation of an angle θ (in degrees) towards the [100] and [010] directions, respectively (Fig. 3 - right). We have also performed additional simulations with misorientation axis within the $(1\bar{1}0)$ plane (not shown). In these cases, the [100] and [010] directions remain equivalent, and no significant differences have been observed with the microstructure evolution under perfect [110] loading.

The cuboidal microstructure is submitted to a constant uniaxial stress of $\sigma^a = 150$ MPa while holding the temperature at $950°$C. In these conditions, plasticity is only active inside the γ channels, whereas the γ' phase behaves elastically [7]. The simulations are realized using both the elastic and full elasto-viscoplastic model presented in Section 2 with the material parameters listed in Tables 1 and 2. Only the elasto-viscoplastic results are presented in details here. The same initial homogeneous dislocation density on all slip systems $\rho_0^\alpha = \bar{\rho}_0 = 2.6 \ 10^{12} \ \text{m}^{-2}$ has been considered [49, 50].

In Figures 1-b and 1-c, the microstructure obtained after $t = 25.5$ min under the perfect [110] and the [110]$+12°$ oriented load are presented, respectively, using concentration fields. Their respective autocorrelation functions are also shown below each concentration field.

For the perfect [110] tensile load, the applied stress mainly leads to the coarsening of the precipitates along the [001] crystal orientation to form a microstructure made of rod-like precipitates elongated in a direction perpendicular to the tensile loading axis. First, the formation of rods by the merging of precipitates along [001] can be inferred from the autocorrelation function in Fig. 1-b (blue curve), where the local maximum I_1 along the [001], characteristic of the microstructure periodicity, has disappeared. We have observed that it is no longer visible after about $t = 4$ min (not shown). Second, the precipitate shape evolution can be seen in Fig. 2-a, where the characteristic precipitate length L_2 along the [001] is shown to steadily increase during the whole simulation, while L_2 along [100] and [010], first decrease within the first 5 minutes before reaching a nearly constant value. Note that we observe during the first few minutes a rapid precipitate shrinkage along [100] and [010] and the merging of the precipitates along [001] then the precipitates barely evolve along [100] and [010] but they keep on elongating slowly along [001].

A qualitatively different result is obtained when a misorientation is introduced ($\theta = +12°$). Indeed, a microstructure made of rafts with a normal along [010] is formed by the coarsening of the precipitates along the [100] and [001] directions. This microstructure evolution is clearly visible in the autocorrelation functions (Fig. 1-c), with two monotonously decreasing curves along [100] and [001], and the existence of a strong local maximum $I_1^{[010]}$ along [010] (green curve). Note that the local maximum $I_1^{[001]}$ disappears very rapidly ($t = 3$ min, not shown), whereas $I_1^{[100]}$ only slowly disappears and is still visible at t = 25.5 min (red curve in Fig. 1-c). In addition, the precipitate shape change during the raft formation can be deduced from the evolution of the characteristic length L_2. As shown in Fig. 2-b, the evolution of L_2 in the [010] and [001] direction behaves similarly as for the [110] applied load (Fig. 2-a), whereas the evolution of $L_2^{[100]}$ is qualitatively different: after a small initial decrease, a monotonous increase is observed. This leads to the formation of plate-like precipitates normal to the [010] direction.

Note also that the strong elongation of the precipitate along the [001] direction in Fig. 2 is observed whatever the value of the misorientation. This point will be used in the following section to analyse the later stages of the microstructure evolution using two-dimensional simulations.
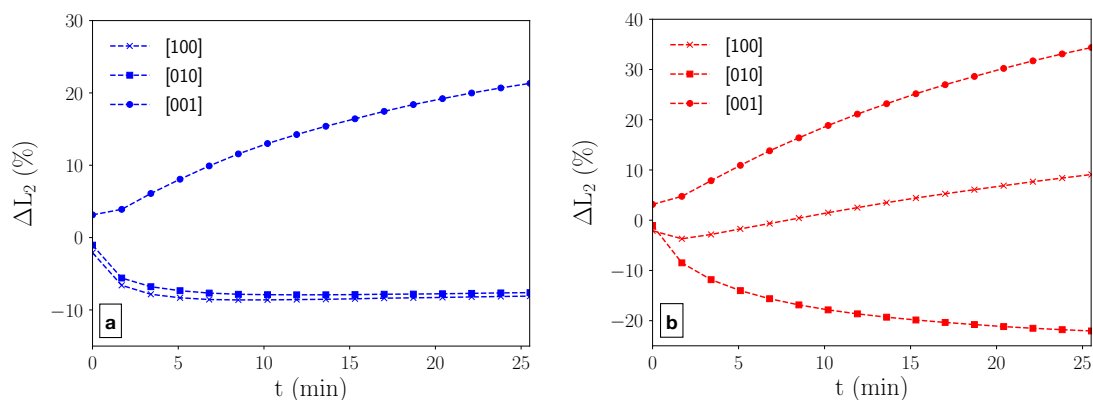

Figure 2: Evolution of $\Delta L_2(t) = (L_2(t) - L^0)/L^0$ in the three cubic directions for the a - [110] and b - [110]$+12°$ applied load.

The consequences of plasticity on the microstructure evolution have been analyzed by performing the same simulations without activating plasticity (not shown). For the [110] applied load, there are no significant differences up to $t = 12$ min, then the subsequent rod elongation is faster in the purely elastic simulation. For the [110]+12° load, the elongation rates of the precipitates along the [100] and [001] directions to form rafts are increased by plasticity during the first few minutes. At later times, the main consequence of plasticity is to slow down the precipitate elongation along the [100] direction. The only other significant difference between elastic and elasto-viscoplastic simulations is in the curvature of the precipitates/matrix interfaces being more pronounced in the elastic case. The relative role of elastic and plastic driving forces will be discussed in more detail in §3.2.

In summary, starting from a cuboidal structure, our simulations predict the formation of a microstructure made of rod-like precipitates (elongated in the [001] direction) under a tensile creep load along the [110] direction. In addition, a small misalignment of the loading axis from the [110] direction ($\theta = +12°$) is shown to induce the formation of rafts with a coarsening of the precipitates successively in the [001] and [100] directions. This point confirms that the formation of rafts during [110] creep loading can be explained by slight misorientations of the traction axis. Finally, the elasto-viscoplastic phase field simulations carried out by Gaubert et al. [26] on a very simplified microstructure containing a single precipitate (with periodic boundary conditions) showed an elongation of the precipitate in the [001] direction, but rafting was not observed, even for misoriented traction axis. Although this work relies on a different crystalline plasticity model, the comparison with our results strongly suggests that imperfections of shape, size and alignment of the cuboidal precipitates are necessary to obtain rafts.
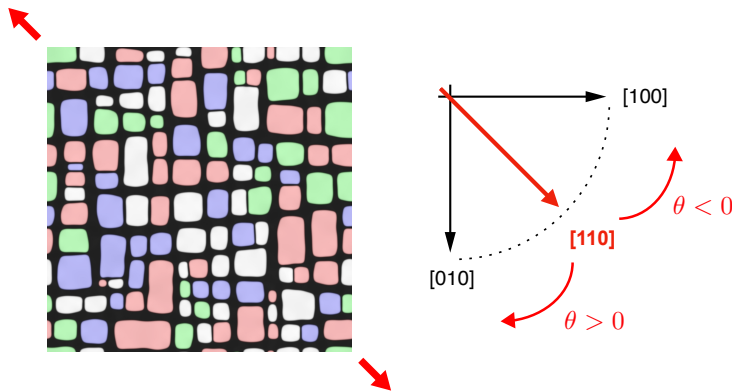
3.2. 2D rafting of Ni-based superalloys during creep

Figure 3: Left: Initial microstructure (colors indicate γ' variants) in 4.6^2 µm² periodic box. Red arrows represent the applied stress for the perfect [110] crystal orientation. Right: Diagram of the different misorientations applied to the microstructure.

To go further in our investigation, several 2D simulations are computed since the 3D cuboidal structure quickly coarsen along the [001] to form rods or platelets. As a result, we can realistically analyse the subsequent microstructure evolution under [110] creep loading by realising 2D calculations in the (001) plane. Furthermore, as they are less time-consuming a systematic study is now within reach on different misorientations, and on longer timescales. Our results will also give us insights into the respective role of the elastic and plastic driving forces during the evolution. Then, the mechanical behavior will be investigated as well as the impact of the initial plastic state of the microstructure on the following evolution.

3.2.1. 2D rafting with full elasto-viscoplastic model

The influence of different misorientations θ is now investigated during microstructure evolution under [110]+θ creep load using the full elasto-viscoplastic model presented in Section 2. 2D simulations of 4.6^2 µm² discretized with 1024^2 nodes are performed.
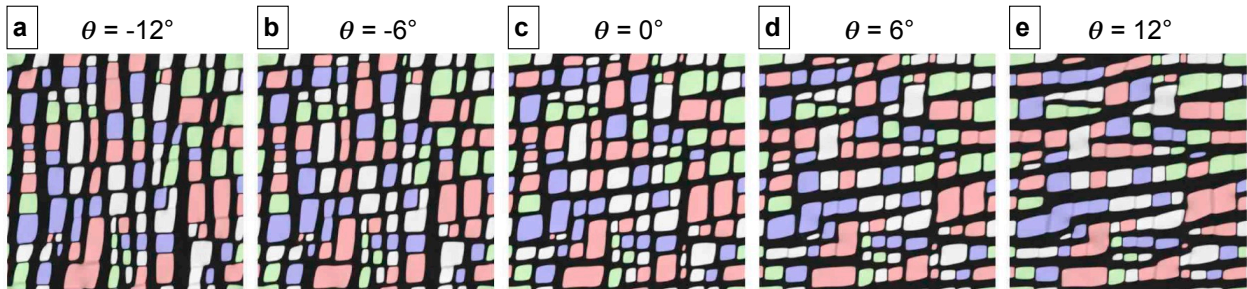
Figure 4: Microstructures obtained at $t = 7.6$ h with an inhomogenous elasto-viscoplastic simulation for several misorientations θ of the loading axis a) -12°, b) -6°, c) 0°, d) +6°, e) +12°.

In a first step, starting from an initial disordered γ phase, the alloy is aged during 4.2 h at 950°C under stress-free conditions using the elastic phase field model parametrized with the material parameters listed in Table 1. The resulting microstructure consists of γ' cuboidal precipitates, as shown in Fig. 3 where the colors represent represent the four translational variants of γ', aligned along cubic directions and separated by well-defined γ channels (dark regions). The volume fraction of the γ' precipitates is $f_v = 0.62$. The aspect ratio of each precipitate can be determined as the ratio between the smallest and largest lengths of the precipitate along the cubic directions. These lengths are defined as quadratic standard deviations from the central position of the precipitate following Cottura et al. [46]. Using these measurements, we have characterized quantitatively the shape of the precipitates by the average aspect ratio $\langle \ell_{min}/\ell_{max} \rangle$. In the microstructure in Fig. 3, the precipitates average size is around 350 nm with an average aspect ratio of 0.77 reflecting their cuboidal morphology, while the γ channels are around 95 nm wide.

In a second step, a constant uniaxial stress of $\sigma^a = 150$ MPa is applied to the microstructure while holding the temperature at 950°C. The orientation of σ^a is chosen with different misorientation angles θ from the perfect [110] orientation such as $\theta = -12°, -6°, 0°, +6°, +12°$ (Fig. 3 - right). For each case, the calculations are performed using the full elasto-viscoplastic model considering the material parameters listed in Tables 1 and 2, as well as the same initial dislocation density on all slip systems $\bar{\rho}_0 = 2.5 \ 10^{12} \ m^{-2}$ in agreement with experimental assessments [49, 50].

In Fig. 4, snapshots of the final microstructure after 7.6 h under [110]+θ creep load are presented. Consistent with the previous 3D results, we observe a microstructure made of cuboids under a perfect [110] load (Fig. 4-c) and the formation of elongated precipitates/rafts when a misorientation θ from [110] is considered (Fig. 4-a-b-d-e). The results show that the sign of θ selects the orientation of the rafts: when $\theta < 0$, vertical elongated precipitates are obtained, whereas they are horizontal for $\theta > 0$. Note that in each case, precipitates are not perfectly aligned with the cubic directions. This point will be further detailed in the following section (§3.2.2). In addition, even though $\theta \leftrightarrow -\theta$ misorientations should lead to equivalent results by symmetry, a stronger alignment with the cubic directions is observed for the vertical rafts (Fig. 4-a-b). This is a consequence of the initial microstructure i.e. the initial alignment and distribution of precipitate variants, which breaks this symmetry and significantly impact the subsequent development of the rafts. However, we verified that the average characteristic quantities of the microstructure (volume fraction, number and average size of precipitates, average aspect ratio) are almost equal in the $\pm\theta$ simulations. Finally, we note that the rafts are more developed for large misorientations. We also verified that rafting increases with the misorientation (not shown) as in-phase precipitates aligned in the appropriate direction coagulate more easily. We have also performed several other simulations with misorientation axis within the [1$\bar{1}$0] plane (not shown). In these cases, [100] and [010] directions remain equivalent, and we observed no significant difference with the microstructure evolution under perfect [110] loading.

3.2.2. Analysis of the elastic driving force for rafting

Starting from the cuboidal microstructure presented in Fig. 3, we now analyze the role of the elastic driving force by performing simulations without plasticity (Fig. 5).
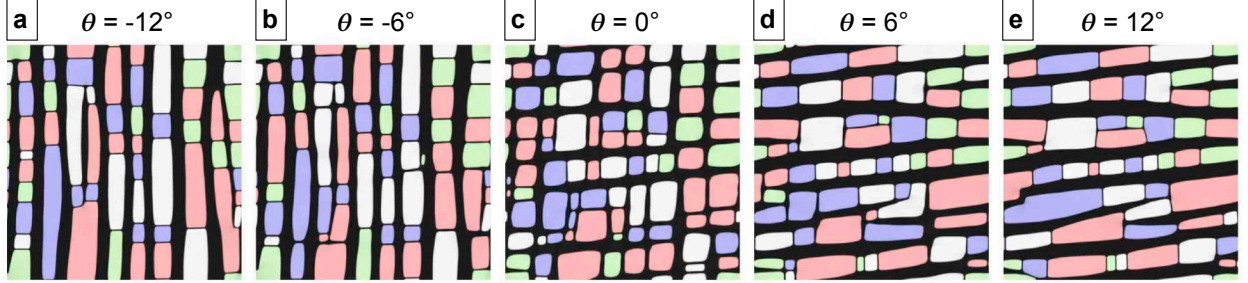

Figure 5: Microstructures obtained at $t = 7.6$ h with an inhomogenous elastic simulation with no plasticity for several misorientations θ of the loading axis a) -12°, b) -6°, c) 0°, d) +6°, e) +12°.

Figure 5-c shows the microstructure obtained at t = 7.6 h under a perfect [110] load. A coarsening of the microstructure is observed: the average precipitate size increases, mainly by Ostwald ripening where large precipitates grow at the expense of smaller ones by exchanging solute by diffusion through the matrix. When in-phase neighboring precipitates grow, very few coagulations take place as a high inhomogeneity on the shear elastic constant $C' = (C_{11} - C_{12})/2$ ($\Delta C' = 40\%$ here) inhibits such events in a microstructure with a high volume fraction of γ' [46]. During this coarsening, the precipitates remain cuboidal with an aspect ratio of 0.75 and tend to align along two directions, which are close to the horizontal and vertical directions, without forming rafts. The orientation of the precipitates alignment is about 5° away from the cubic directions.

The orientation of the precipitate interfaces and the direction of their alignment can be analytically related to the elastic inhomogeneity and to the applied stress. Indeed, as detailed in Appendix A, using a mean field approximation, the problem with an inhomogeneous elasticity under an applied stress, is equivalent to a problem of homogeneous elasticity with an effective eigenstrain. For a [110] loading axis, the effective eigenstrain $\underset{\sim}{\boldsymbol{\epsilon}}^*$ is

$$\epsilon^*_{11} = \epsilon^*_{22} = \epsilon^0 - \frac{\sigma^a}{12} \frac{\Delta C'}{\bar{C}'^2} \tag{14}$$

$$\epsilon^*_{33} = \epsilon^0 + \frac{\sigma^a}{6} \frac{\Delta C'}{\bar{C}'^2} \tag{15}$$

$$\epsilon^*_{12} = -\frac{\sigma^a}{4} \frac{\Delta C_{44}}{(\bar{C}_{44})^2} \tag{16}$$

where $\bar{C}_{11}$, $\bar{C}_{12}$, $\bar{C}_{44}$ are the spatially averaged elastic constants, and where we have used the fact that the contribution of the inhomogeneity of the bulk modulus is negligible.

We first analyze the consequences of an elastic inhomogeneity on the shear moduli C'. When $\sigma^a \Delta C' \epsilon_0 < 0$[1], as it is the case in this work, we have $|\epsilon^*_{11}| = |\epsilon^*_{22}| > |\epsilon^*_{33}|$. Therefore, (100) and (010) interfaces are elastically favored compared to (001) interfaces, which is consistent with the elongation of the microstructure along the [001] direction. If a small inhomogeneity ΔC_{44} is added, off-diagonal terms appear in the effective

---

[1]When $\sigma^a \Delta C' \epsilon_0 > 0$, (001) interfaces are elastically favorable and rafts perpendicular to [100] are expected.

eigenstrain. Therefore, the optimal orientations of the interfaces are expected to deviate from the cubic plane. This is consistent with the observation of a $5°$ angular deviation angle away from the cubic directions in Figure 5-c. It can be noticed that the elastic soft directions can also be obtained as the orientations which minimize the elastic potential of a γ/γ' one dimensional laminate. These numerical calculations (not shown), performed with inhomogeneous elastic constants, confirm the rôle of the elastic inhomogeneity $\Delta C'$ and ΔC_{44} obtained from the analysis of the effective eigenstrain.

We now analyze the microstructure as a function of the misorientation with respect to [110] axis. As shown in Figure 5, we observe that the introduction of a non zero misorientation leads to the formation of rafts, consistently with 3D simulations. When $\theta < 0$, i.e. a loading axis closer to [100], elongated precipitates with a normal along [100] are obtained whereas their normal is along [010] for $\theta > 0$. While for $\theta = 0$ the aspect ratio of the precipitates remains around 0.75, for $|\theta| > 0$ it drops down to around 0.59, in agreement with the formation of platelets and rafts. Even with a small misorientation of $|\theta| = 3°$ (not shown), microstructure evolution is significantly modified: precipitates are already more elongated with an aspect ratio of 0.66 even if rafts are not formed yet.

The consequences of the misorientation can be explained by the mean field approximation. Indeed, the introduction of a small misorientation θ changes the applied stress by the following quantity:

$$\delta \underset{\approx}{\boldsymbol{\sigma}}_\theta^a = -\sigma^a \sin\theta \begin{pmatrix} \cos\theta & \sin\theta & 0 \\ \sin\theta & -\cos\theta & 0 \\ 0 & 0 & 0 \end{pmatrix} \approx -\sigma^a \theta \begin{pmatrix} 1 & 0 & 0 \\ 0 & -1 & 0 \\ 0 & 0 & 0 \end{pmatrix} \tag{17}$$

The right-hand side expression of Eq. 17 belongs to the Kelvin mode related to $C_{11} - C_{12} = 2C'$ (see Appendix A). The change of the effective eigenstrain due to the small misorientation θ is therefore:

$$\delta \underset{\approx}{\boldsymbol{\epsilon}}^* = 2\,\sigma^a \theta\, \frac{\Delta C'}{\bar{C}'^2} \begin{pmatrix} 1 & 0 & 0 \\ 0 & -1 & 0 \\ 0 & 0 & 0 \end{pmatrix} \tag{18}$$

From this expression, it appears that the consequences of a small misorientation is related to the inhomogeneity $\Delta C'$. In the case considered in this paper where $\sigma^a \Delta C' \epsilon_0 < 0$, we have seen that (100) and (010) interfaces are both elastically favored when the loading axis is exactly [110]. The eigenstrain increment in Eq. (18) lifts the degeneracy and, if $\theta < 0$, we have $|\epsilon_{11}^*| > |\epsilon_{22}^*| > |\epsilon_{33}^*|$ so that the (100) interfaces are favored. On the contrary, if $\theta > 0$, the (010) interfaces are elastically favored. This conclusion is in agreement with the results presented in Fig. 5.

In brief, for the model superalloy studied in this paper, we have first shown that the elastic driving force favors the raft formation observed in the elastic-viscoplastic simulation (Fig. 4). Then, we have analysed the elastic driving force using a mean field approach. We have shown that the elastic driving force depends on the sign of the applied stress, of the elastic inhomogeneity and the stress free strain. In particular, we have highlighted the importance of the inhomogeneity coefficient $\Delta C'$, which largely controls the elastic soft directions for a [110] loading axis, and which controls the raft orientation when a misorientation θ is introduced.

3.2.3. Analysis of plasticity under [110] creep load

In this section, we first describe the main differences on the microstructure evolution when plasticity is accounted for. Then, we analyze the operating dislocation slip systems, starting with a perfect [110] loading axis, followed by a loading along [110]+12°.

When comparing Fig. 4 and Fig. 5, it appears that after t=7.6 h, the rafting is more developed for the elastic simulation. It can be explained by the slow rafting kinetics when plasticity is accounted for as it has already been observed for [100] creep [27, 28]. Indeed, whereas the number of precipitates is cut-down in more than half in the elastic case, it only decreases by around 25% at most ($\theta = +12°$) for the elasto-viscoplastic

ones. In the latter case, the average size of the γ' precipitates slightly decreases to 310 nm, and the volume fraction behaves similarly. In addition, careful analysis reveals that the interfaces are slightly different when plasticity is accounted for. The normal to the rafts rotates towards the tensile loading axis in agreement with the results obtained in Gaubert et al. [26].

Under a [110] load, 4 out of the 12 glide systems of the fcc crystal are activated: B2, B4 , C1 and C3 (Schmid & Boas notation). As the systems are not collinear, we expect only a small influence of the hardening matrix on the microstructure evolution. In our simulations, all the active slip systems evolve almost identically, therefore only the evolution of the average dislocation density are presented in Figure 6 (full grey curve). Moreover, B2 & C1 are only active in the γ channels with a normal along [010], whereas B4 & C3 are only active in the γ channels with a normal along [100] (as schematized in Fig. 6).
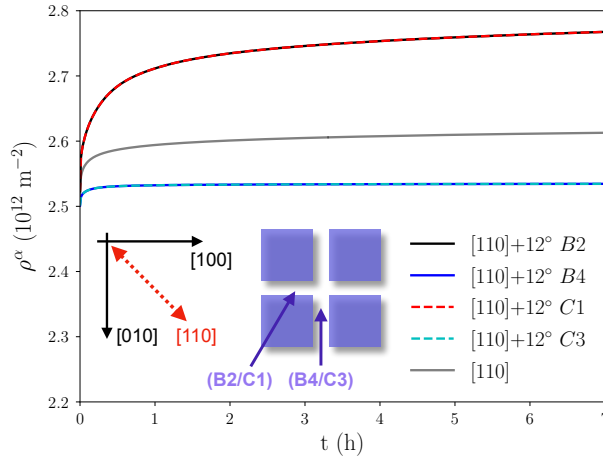

Figure 6: Time evolution of the dislocation densities ρ^α for different directions of the applied load.

By assessing the elastic stresses in the initial cuboidal microstructure, we can understand the activation of the glide systems in our simulations. When the γ channels are very thin because of the high volume fraction of precipitates, the stress tensors $\boldsymbol{\sigma}_{c[100]}$ and $\boldsymbol{\sigma}_{c[010]}$ inside the channels with normals along [100] and [010], respectively, can be assumed constant and expressed as:

$$
\boldsymbol{\sigma}_{c[100]} = \begin{pmatrix} \sigma_1 + \sigma^a/2 & \sigma^a/2 & 0 \\ \sigma^a/2 & \sigma_2 + \sigma^a/2 & 0 \\ 0 & 0 & \sigma_2 \end{pmatrix} \quad ; \quad \boldsymbol{\sigma}_{c[010]} = \begin{pmatrix} \sigma_2 + \sigma^a/2 & \sigma^a/2 & 0 \\ \sigma^a/2 & \sigma_1 + \sigma^a/2 & 0 \\ 0 & 0 & \sigma_2 \end{pmatrix} \tag{19}
$$

where (σ_1, σ_2) are the non-zero components of the coherency stress and σ^a is the applied stress. A rough estimate from the simulations (or considering 1D laminate elastic calculations) gives $\sigma_1 \approx 0$ and $\sigma_2 \approx 50$ MPa for the stresses inside the channels generated by the microstructure under stress-free conditions. From this estimate, in the channels with a normal along [010], the primary slip systems are B2 & C1 which are associated with the resolved shear stress $\sigma_r = (\sigma_2 - \sigma_1 - \sigma^a)/\sqrt{6}$. In the channels with a normal along [100], the primary slip systems are B4 & C3 with the same σ_r. All the other slip systems feature lower σ_r.

As seen in Figure 6, when a misorientation [110]+θ is considered, the systems B2/C1 (black/red curve) are differentiated from B4/C3 (dark/light blue curve). For $\theta = +12°$, after a rapid increase, the average dislocation densities on B2/C1 reach a higher value $\bar{\rho} = 2.76 \ 10^{12} \ \mathrm{m}^{-2}$ compared to $\bar{\rho} = 2.53 \ 10^{12} \ \mathrm{m}^{-2}$ in the glide systems B4/C3. We observe that plasticity happens mainly in the channels that are formed during rafting: the horizontal ones for $\theta > 0$.

An analysis similar to the one proposed for the [110] perfect load can be performed but the applied stress tensor is now modified by the quantity $\delta\boldsymbol{\sigma}_\theta^a$ defined in Eq. (17). For the systems B2 & C1 in the [010] channels, the additional stress modifies the resolved shear stress σ_r by $\sigma_a \sin\theta(\sin\theta - \cos\theta)$. As $\sigma_r < 0$ for $\theta = 0$, it means that a misorientation $\theta > 0$ leads to an increase of σ_r in absolute value and thus plasticity is expected to be favored. On the contrary, $\theta < 0$ leads to a decrease in absolute value of σ_r. For the systems B4 & C3 in the [100] channels, the additional stress modifies σ_r by $\sigma_a \sin\theta(\sin\theta + \cos\theta)$. It means that when $\theta > 0$ $|\sigma_r|$ decreases, whereas when $\theta < 0$ $|\sigma_r|$ increases and plasticity is favored. Therefore, when $\theta > 0$, we predict that plasticity will develop more easily in the [010] channels (glide systems B2 & C1) than in the [100] channels (glide systems B4 & C3). This prediction is consistent with our results, and the final orientation of the rafts corresponds to the channels where plasticity most efficiently reduces the local stresses.
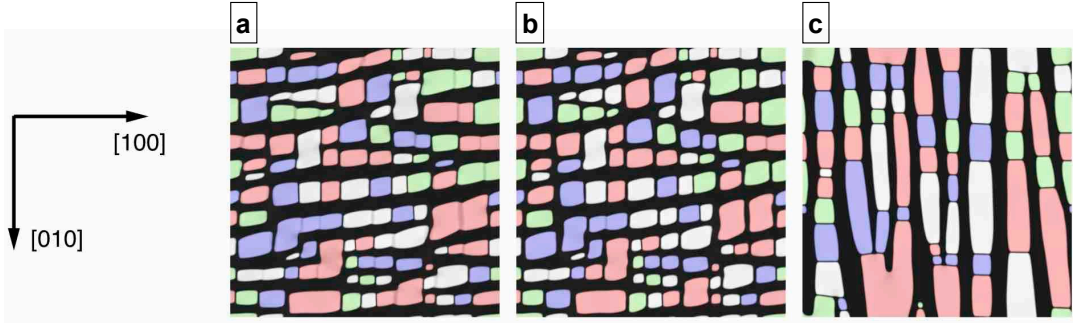
3.2.4. Analysis of the driving forces

Figure 7: Microstructures in a 4.6^2 µm^2 periodic box after $t = 7.6$ h under [110]+12° creep load in: a - the homogeneous elasto-viscoplastic case, b - inhomogeneous elasto-viscoplastic case with switched elastic constants; c - inhomogeneous elastic case with switched elastic constants.

In this part, we analyze the plastic driving force for rafting using two model cases. First, we have performed a simulation in which the elastic driving force for rafting is removed. The latter resulting from elastic inhomogeneity, we have simply set the elastic constants of the γ and γ' phases to the same value. The results are shown in Fig 7-a, where we have used the elastic constants of the γ phase and a misorientation $\theta = +12°$. The obtained microstructure is rafted, indicating that plasticity alone induces rafting when some misorientation is present. In addition, Figures 7-a and 4-e are very similar suggesting that the plastic driving force is dominant. We have confirmed this point by performing two simulations where we have switched the elastic constants between the γ and γ' phases. This does not modify significantly the plastic driving force whereas it changes the sign of the elastic one. The change is clearly visible in the purely elastic simulation presented in Fig. 7-c, where vertical rafts are observed with $\theta = +12°$ instead of the horizontal ones shown in Fig. 5-e. The elasto-viscoplastic simulation represented in Fig. 7-b clearly demonstrates that the raft orientation is dictated by the plastic driving force as horizontal rafting is observed. Even if this result is not general, the model is clearly adapted to investigate the respective influence of the driving forces on microstructure evolution on a specific alloy.

3.2.5. Macroscopic mechanical behavior

In Fig. 8, the average plastic strain $\varepsilon_{\vec{T}}^P$ evolution along the tensile direction $\vec{T}$ is plotted for the [110] creep load. A primary creep stage featuring a rapid increase of $\varepsilon_{\vec{T}}^P$ is observed when $t < 1$ h. Then, the evolution slows down and becomes almost linear to reach about 0.061% after 7 h (green curve). During this secondary creep stage, the microstructure barely evolves. Finally, Figure 8 also reports the evolution of $\varepsilon_{\vec{T}}^P$ for the two positive misorientations $\theta = +6°$ and $+12°$. The overall behavior is qualitatively similar to the perfect [110] load with a rapid primary creep stage followed by an almost linear and slow secondary stage. Note that at
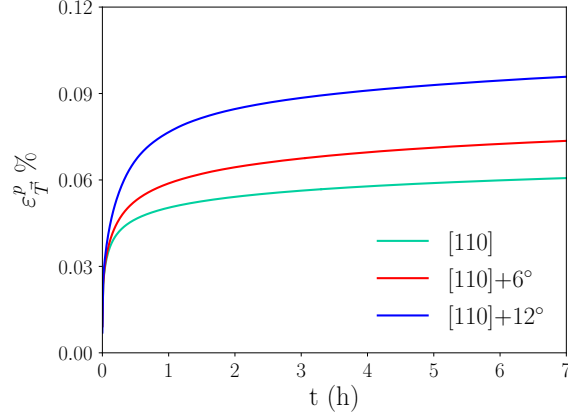
14

Figure 8: $\varepsilon_{\vec{T}}^P$ along the tensile direction vs time for different applied loads and an initial dislocation density of $\bar{\rho}_0 = 2.5 \; 10^{12} \; \text{m}^{-2}$.

the end of the primary creep stage, a rafted microstructure is observed for both misorientated cases while the perfect [110] displays a cuboidal structure. Plasticity develops faster for an increasing misorientation with values around 0.074% and 0.096% after 7 h for $\theta = +6/+12°$ (red and blue curves), respectively. It is consistent with a faster formation of well-defined rafted structure (Fig. 4-d-e).

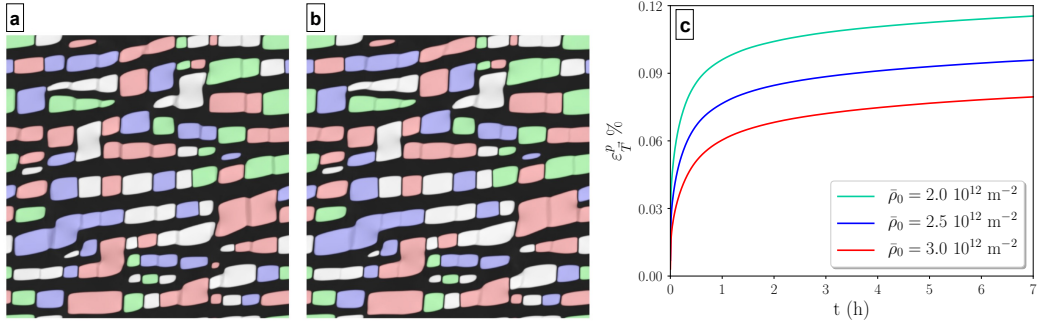Figure 9: Snapshots of the final microstructure after $t = 7.6$ h under [110]+12° creep load: a - $\bar{\rho}_0 = 2 \times 10^{12} \; \text{m}^{-2}$ and b - $3 \times 10^{12} \; \text{m}^{-2}$; c - corresponding evolution of the average plastic strain $\varepsilon_{\vec{T}}^P$.

Finally, we look into the influence of the initial dislocation density on the subsequent microstructure evolution. It is generally difficult to measure precisely dislocation densities in materials. Therefore, it is important to assess how our previous results are affected by this parameter. As before, we focus on the case of rafting under a [110]+12° tensile load using the full elasto-viscoplastic model. Figure 9-a-b shows the microstructures obtained for a variation of ±20% of the initial dislocation density $\bar{\rho}_0$ employed previously. Rafts are slightly more developed when employing a higher initial dislocation density but overall microstructure evolution is barely modified. However, the macroscopic mechanical behavior is significantly impacted, as shown in Fig. 9-c, with both the primary and secondary creep stages exhibiting differences. A lower initial dislocation density induces a faster increase of the plastic strain during primary creep resulting in a more deformed material. Indeed, a higher value is reached with $\varepsilon_{\vec{T}}^P = 0.11\%$ (green curve) compared to 0.08% for the higher initial density at the end of the treatment (red curve).

15

4. Conclusion

We have investigated the microstructure evolution under [110] creep load in a model superalloy is realized. We used a Phase Field model coupled to a dislocation density based crystal plasticity model we previously developed. It accounts for the anisotropy as well as the size-dependence of the plastic activity, which is expected when plasticity is confined in region below few microns in size. It also includes a storage-recovery law for the dislocation density of each glide system and a hardening matrix to account for the short-range interactions between dislocations. The model is used to address the microstructural evolution in Ni-based superalloys in creep conditions during which plasticity only proceeds inside the γ phase. Most of the important physical phenomena, such as the presence of different crystallographic γ' variants, their misfit with the γ matrix, the elastic inhomogeneity and anisotropy, the hardening, anisotropy and viscosity of plasticity are included.

First, 3D simulations of microstructure formation and evolution in Ni-based superalloys during creep with tensile loads close to the [110] are performed. Starting from a cuboidal structure, our simulations lead to the formation of a microstructure made of rod-like precipitates under a constant stress along the perfect [110] direction. Our results also show that a small misalignment from this axis is required to observe rafting of the precipitates as it has been observed experimentally. First, a rapid coarsening along the direction [001] perpendicular to the applied load is observed, then platelets are formed using a purely elastic or a full elasto-viscoplastic model.

Note also that the autocorrelation function employed to analyse our results is well-suited to describe and quantify changes in microstructure evolution. It is particularly useful for 3D simulations where microstructural changes might be hard to distinguish considering the number of events ; in our case, it gives the possibility to i) distinguish between cuboidal, rod and platelet precipitates, ii) quantify the precipitate size evolution and iii) understand and quantify the coarsening kinetics.

Second, the analysis of the 3D calculations has justified the use of 2D settings for investigating systematically the influence of misorientation, reaching longer durations with more established rafts. Several results were obtained: even a deviation as small as 3° modifies the microstructure evolution, a larger misorientation leads to more developed rafts and the direction of misorientation with respect to the perfect [110] axis selects the rafting direction. Our analysis of the elastic and plastic driving forces when a misorientation is accounted for also shows that (i) the inhomogeneity of the shear elastic constants C' influences the rafts orientation, (ii) inhomogeneous elasticity or plasticity alone are enough to generate rafts and (iii) in our material plasticity is the main driving force for rafting. Finally, the choice of initial dislocation density modify only slightly the following microstructure evolution but has a strong impact on the macroscopic behavior of the material.

Appendix A.

Following [29, 51], within a mean-field approximation and as long as the configuration-dependent elastic energy is involved, a problem of inhomogeneous elasticity under external load can be mapped into a problem of homogeneous elasticity without external stress and characterized by an effective eigenstrain given by:

$$\underset{\sim}{\epsilon}^* = \underset{\sim}{\epsilon}^0 + (1 - 2f_v)\underset{\approx}{\bar{S}} : \underset{\approx}{\Delta\lambda} : \underset{\sim}{\epsilon}^0 - \underset{\approx}{\bar{S}} : \underset{\approx}{\Delta\lambda} : \underset{\sim}{\bar{\epsilon}} \tag{A.1}$$

where f_v is the volume fraction of precipitates, $\underset{\sim}{\epsilon}^0$ the eigenstrain of the precipitate and $\underset{\sim}{\bar{\epsilon}}$ the average strain. $\underset{\approx}{\bar{S}}$ is the compliance tensor corresponding to the spatially averaged elastic tensor, and $\underset{\approx}{\Delta\lambda}$ is the difference between the precipitate and matrix elastic tensors.

If the condition $|\underset{\sim}{\sigma}^a| \gg |\underset{\approx}{\Delta\lambda}||\underset{\sim}{\epsilon}^0|$ is fulfilled, the average strain $\underset{\sim}{\bar{\epsilon}}$ can be easily approximated and we get

$$\underset{\sim}{\epsilon}^* = \underset{\sim}{\epsilon}^0 + (1 - 2f_v)\underset{\approx}{\bar{S}} : \underset{\approx}{\Delta\lambda} : \underset{\sim}{\epsilon}^0 - \underset{\approx}{\Gamma} : \underset{\sim}{\sigma}^a \tag{A.2}$$

where the tensor $\underset{\approx}{\mathbf{\Gamma}}$ is defined by

$$\underset{\approx}{\mathbf{\Gamma}} = \bar{\mathbf{S}} : \Delta \underset{\approx}{\mathbf{\lambda}} : \bar{\mathbf{S}} \tag{A.3}$$

In the case of Ni-based superalloys the precipitate and matrix have the same cubic symmetry, therefore the above tensor can be easily computed in the Kelvin basis, which is common to the two phases [52]. More precisely, we use the following basis:

$$e_1 = \frac{1}{\sqrt{3}} \begin{bmatrix} 1 & 0 & 0 \\ 0 & 1 & 0 \\ 0 & 0 & 1 \end{bmatrix} \quad ; \quad e_2 = \frac{1}{\sqrt{2}} \begin{bmatrix} 1 & 0 & 0 \\ 0 & \bar{1} & 0 \\ 0 & 0 & 0 \end{bmatrix} \quad ; \quad e_3 = \frac{1}{\sqrt{6}} \begin{bmatrix} 1 & 0 & 0 \\ 0 & 1 & 0 \\ 0 & 0 & \bar{2} \end{bmatrix} \tag{A.4}$$

$$e_4 = \frac{1}{\sqrt{2}} \begin{bmatrix} 0 & 1 & 0 \\ 1 & 0 & 0 \\ 0 & 0 & 0 \end{bmatrix} \quad ; \quad e_5 = \frac{1}{\sqrt{2}} \begin{bmatrix} 0 & 0 & 0 \\ 0 & 0 & 1 \\ 0 & 1 & 0 \end{bmatrix} \quad ; \quad e_6 = \frac{1}{\sqrt{2}} \begin{bmatrix} 0 & 0 & 1 \\ 0 & 0 & 0 \\ 1 & 0 & 0 \end{bmatrix} \tag{A.5}$$

e_1 is the eigenvector of $\underset{\approx}{\mathbf{\lambda}}$ associated with eigenvalue $C_{11} + 2C_{12}$; e2 and e3 are the eigenvectors associated with the multiple eigenvalue $C_{11} - C_{12}$; and e4, e5 and e6 are the eigenvectors associated with the multiple eigenvalue $2C_{44}$.

In the case of uniaxial loading along the [110] direction, we get:

$$\epsilon_{11}^* = \epsilon_{22}^* = \tilde{\epsilon}^0 - \frac{\sigma^a}{2} \left(\frac{2}{3} \frac{\Delta C_{11} + 2\Delta C_{12}}{(\bar{C}_{11} + 2\bar{C}_{12})^2} + \frac{1}{3} \frac{\Delta C_{11} - \Delta C_{12}}{(\bar{C}_{11} - \bar{C}_{12})^2} \right) \tag{A.6}$$

$$\epsilon_{33}^* = \tilde{\epsilon}^0 - \frac{\sigma^a}{2} \left(\frac{2}{3} \frac{\Delta C_{11} + 2\Delta C_{12}}{(\bar{C}_{11} + 2\bar{C}_{12})^2} - \frac{2}{3} \frac{\Delta C_{11} - \Delta C_{12}}{(\bar{C}_{11} - \bar{C}_{12})^2} \right) \tag{A.7}$$

$$\epsilon_{12}^* = -\frac{\sigma^a}{2} \left(\frac{2\Delta C_{44}}{(2\bar{C}_{44})^2} \right) \tag{A.8}$$

where

$$\tilde{\epsilon}^0 = \epsilon^0 \left(1 + (1 - 2f_v) \frac{\Delta C_{11} + 2\Delta C_{12}}{\bar{C}_{11} + 2\bar{C}_{12}} \right) \tag{A.9}$$

In the present work, the contribution of the inhomogeneity of the bulk modulus (i.e. $\Delta C_{11} + 2\Delta C_{12} \approx 0$) is negligible so the effective eigenstrain reduces to:

$$\epsilon_{11}^* = \epsilon_{22}^* = \epsilon^0 - \frac{\sigma^a}{6} \frac{\Delta C_{11} - \Delta C_{12}}{(\bar{C}_{11} - \bar{C}_{12})^2} \tag{A.10}$$

$$\epsilon_{33}^* = \epsilon^0 + \frac{\sigma^a}{3} \frac{\Delta C_{11} - \Delta C_{12}}{(\bar{C}_{11} - \bar{C}_{12})^2} \tag{A.11}$$

$$\epsilon_{12}^* = -\frac{\sigma^a}{4} \frac{\Delta C_{44}}{(\bar{C}_{44})^2} \tag{A.12}$$

References

[1] T. Khan, P. Caron, Effect of heat treatment on the creep behavior of a Ni-base single crystal superalloy, in: J. Bilde-Sorensen, N. Hansen, A. Horsewell, T. Leffers, H. Lilholt (Eds.), Deformation of Multi-Phase and Particle Containing Materials, Riso National Laboratory (1983) 333–338.

[2] J. Tien, S. Copley, The effect of uniaxial stress on the periodic morphology of coherent gamma prime precipitates in nickel-base superalloy crystals, Metall. Trans. 2 (1971) 215–219.

[3] J. Tien, S. Copley, The effect of uniaxial stress on the periodic morphology of coherent gamma prime precipitates in nickel-base superalloy crystals, Metall. Trans. 2 (1971) 543–553.

[4] A. Royer, P. Bastie, M. Véron, *In situ* determination of γ' phase volume fraction and of relations between lattice parameters and precipitate morphology in Ni-Based single crystal superalloy, Acta Mater. 46 (1998) 5357–5368.

[5] T. Khan, P. Caron, Y.G. Nakagawa, Mechanical Behavior and Processing of DS and Single Crystal Superalloys, JOM 38 (1986) 16–19.

[6] T. Kuttner, M. Feller-Kniepmeier, TEM investigation of the microstructure in a single crystal nickelbase superalloy creep tested in [011] orientation, J. Phys. IV France 03 (1993) C7-325–C7-330.

[7] T. Kuttner, M. Feller-Kniepmeier, Microstructure of a nickel-base superalloy after creep in [011] orientation at 1173 K, Mater. Sci. Eng. A 188 (1994) 147–152.

[8] V. Sass, U. Glatzel, M. Feller-Kniepmeier, Anisotropic creep properties of the nickel-base superalloy CMSX-4, Acta Mater. 44 (5) (1996) 1967–1977.

[9] P. Lukas, J. Cadek, V. Sustek, L. Kunz, Creep of CMSX-4 single crystals of different orientations in tension and compression, Mater. Sci. Eng. A 208 (1996) 149–157.

[10] M.G. Ardakani, M. McLean, B.A. Shollock, Twin formation during creep in single crystals of nickel-based superalloys, Acta Mater. 47 (1999) 2593–2602.

[11] S. Tian, Y. Su, L. Yu, H. Yu, S. Zhang, B. Qian, Microstructure evolution of a [011] orientation single crystal nickel-base superalloy during tensile creep, Appl. Phys. A 104 (2011) 643–647.

[12] S. Tian, S. Zhang, C. Li, H. Yu, Y. Su, X. Yu, L. Yu, Microstructure evolution and analysis of a [011] orientation, single-crystal, nickel-based superalloy during tensile creep, Metall. Mater. Trans. A 43 (2012) 3880–3889.

[13] L. Agudo Jacome, P. Nortershuser, J.-K. Heyer, A. Lahni, J. Frenzel, A. Dlouhy, C. Somsen, G. Eggeler, High-temperature and low-stress creep anisotropy of single-crystal superalloys, Acta Mater. 61 (2013) 2926–2943.

[14] G.M. Han, J.J. Yu, Z.Q. Hu, X.F. Sun, Creep property and microstructure evolution of a nickel-base single crystal superalloy in [011] orientation, Mater. Characterization 86 (2013) 177–184.

[15] L. Agudo Jacome, P. Nortershuser, J.-K. Heyer, A. Lahni, J. Frenzel, A. Dlouhy, C. Somsen, G. Eggeler, On the nature of γ' phase cutting and its effect on high temperature and low stress creep anisotropy of Ni-base single crystal superalloys, Acta Mater. 69 (2014) 246–264.

[16] Y. Su, S. Tian, H. Yu, L. Yu, Effect of pre-compressive treatment on creep behavior of a ¡011¿-oriented single-crystal Ni-based superalloy, Scripta Mater. 93 (2014) 24–27.

[17] P. Nörtershäuser, J. Frenzel, A. Ludwig, K. Neuking, G. Eggeler, The effect of cast microstructure and crystallography on rafting, dislocation plasticity and creep anisotropy of single crystal Ni-base superalloys, Mater. Sci. Eng. A 626 (2015) 305–312.

[18] J. Yu, S. Zhang, Q. Zhang, R. Liu, M. Tang, X. Li, Simulation study and experiment verification of the creep mechanism of a nickel-based single crystal superalloy obtained from microstructural evolution, RSC Adv. 109 (2016) 107748-107758.

[19] Y. Le Bouar, A. Loiseau, A.G. Khachaturya, Effect of elastic interaction on the formation of a complex multi-domain microstructural pattern during a coherent hexagonal to orthorhombic transformation, Acta Mater. 46 (1998) 1359–6454.

[20] Y.H. Wen, Y. Wang, L.Q. Chen, Effect of elastic interaction on the formation of a complex multi-domain microstructural pattern during a coherent hexagonal to orthorhombic transformation, Acta Mater. 47 (1999) 4375–4386.

[21] A. Finel, Y. Le Bouar, A. Gaubert, U. Salman, Phase field methods: microstructures, mechanical properties and complexity, Comptes Rendus Physique, 3-4 (2010) 245-256.

[22] G. Boussinot, A. Finel, Y. Le Bouar, Phase-field modeling of bimodal microstructures in nickel-based superalloys, Acta Mater. 57 (2009) 921.

[23] A. Gaubert, A. Finel, Y. Le Bouar, G. Boussinot, Viscoplastic phase field modelling of rafting in Ni base superalloys, in: D. Jeulin, S. Forest (Eds.), Continuum Models and Discrete Systems CMDS 11, Les Presses de l'École des Mines de Paris (2008) 161–166.

[24] N. Zhou, C. Shen, M. Mills, Y. Wang, Large-scale three-dimensional phase field simulation of γ' rafting and creep deformation, Philosophical Magazine B. 90 (1-4) (2010).

[25] A. Gaubert, Y. Le Bouar, A. Finel, Coupling phase field and viscoplasticity to study rafting in Ni-based superalloys, Philosophical Magazine B 90 (1-4) (2010) 375–404.

[26] A. Gaubert, M. Jouiad, J. Cormier, Y. Le Bouar, J. Ghighi, 3-D imaging and phase field simulations of the microstructure evolution during creep tests of $< 011 >$ oriented Ni-based superalloys, Acta Mater. 84 (2015) 237–255.

[27] M. Cottura, B. Appolaire, A. Finel, Y. Le Bouar, Coupling the Phase Field Method for diffusive transformations with dislocation density-based crystal plasticity: Application to Ni-based superalloys, Journal of the Mechanics and Physics of Solids 94 (2016) 473–489.

[28] M. Cottura, Y. Le Bouar, A. Finel, B. Appolaire, K. Ammar, S. Forest, A phase field model incorporating strain gradient viscoplasticity: Application to rafting in Ni-based superalloys, Journal of the Mechanics and Physics of Solids 60 (7) (2012) 1243 – 1256.

[29] G. Boussinot, Y. Le Bouar, A. Finel, Phase-field simulations with inhomogeneous elasticity comparison with an atomic-

scale method and application to superalloys, Acta Materialia 58 (2010) 4170–4181.

[30] P. Franciosi, M. Berveiller, A. Zaoui, Latent hardening in copper and aluminium single crystals, Acta Metallurgica 28 (1980) 273–283.

[31] A. Vattré, Durcissement des superalliages monocristallins des mécanismes physiques à la modélisation continue, Ph.D. thesis, École Nationale Supérieure des Mines de Paris (2009).

[32] C. Teodosiu, J. L. Raphanel, Finite element simulation of the large elastoplastic deformation, in: C. Teodosiu, J. L. Raphanel, F. Sidoroff (Eds.), Large Plastic Deformations - Fundamentals Aspects and Applications to Metal Forming, A. A. Balkema, 1993, pp. 153 – 168.

[33] L. Kubin, B. Devincre, T. Hoc, Modeling dislocation storage rates and mean free paths in face-centered cubic crystals, Acta Mat. 56 (2008) 6040–6049.

[34] L. Nemat-Nasser, S. Ni, T. Okinaka, A constitutive model for fcc crystals with application to polycrystalline OFHC copper, Mechanics of Materials 30 (4) (1998) 325–341.

[35] I. Groma, P. Balogh, Link between the individual and continuum approaches of the description of the collective behavior of dislocations, Materials Science and Engineering A 234–236 (1997) 249–252.

[36] I. Groma, F. F. Csikor, M. Zaiser, Spatial correlations and higher-order gradient terms in a continuum description of dislocation dynamics, Acta Materialia 51 (5) (2003) 1271–1281.

[37] P. L. Valdenaire, Y. Le Bouar, B. Appolaire, A. Finel, Density-based crystal plasticity : from the discrete to the continuum, Phys. Rev. B 93 (21), 214111.

[38] L. P. Evers, W. A. M. Brekelmans, M. G. D. Geers, Non-local crystal plasticity model with intrinsic SSD and GND effects, Journal of the Mechanics and Physics of Solids 52 (2004) 2379–2401.

[39] S. Bergonnier, F. Hild, S. Roux, Local anisotropy analysis for non-smooth images, Pattern Recogn. 40 (2) (2007) 544–556.

[40] A. Epishin and T. Link and P. D. Portella and U. Brückner, Evolution of the γ/γ' microstructure during high-temperature creep of a nickel-base superalloy, Acta mater., 48 (2000) 4169–4177.

[41] V. Caccuri and R. Desmorat and J. Cormier, Tensorial nature of γ'-rafting evolution in nickel-based single crystal superalloys, Acta Materialia 158 (2018) 138–154.

[42] M. Cottura, B. Appolaire, A. Finel, Y. Le Bouar, Plastic relaxation during growth of Widmanstätten plates, Scripta Mat. 108 (2015) 117–121.

[43] A. J. Ardell, V. Ozolins, Trans-interface diffusion-controlled coarsening, Nature Materials 4 (2005) 309–316.

[44] A. Royer, P. Bastie, M. Véron, In situ determination of γ' phase volume fraction and of relations between lattice parameters and precipitate morphology in Ni-based single crystal superalloy, Acta Materialia 46 (1998) 5357–5368.

[45] F. Diologent, P. Caron, T. d'Almeida, A. Jacques, P. Bastie, The $\gamma - \gamma'$ mismatch in Ni based superalloys in situ measurements during a creep test, Nuclear Instruments and Methods in Physics Research B 200 (2003) 346–351.

[46] M. Cottura, B. Appolaire, Y. Le Bouar, A. Finel, Rôle of elastic inhomogeneity in the development of cuboidal microstructures in Ni-based superalloys, Acta Mater. 94 (2015) 15–25.

[47] F. Fujiwara, M. Watanabe, Z. H. N. Nemoto, K. Noumi, T. Simozaki, Measurements of intrinsic diffusion coefficients in Ni_3Al, in: K. O. M. Koiwa, T. Miyazaki (Eds.), International Conference on Solid-Solid Transformations, in JIMIC-3, 1999, pp. 481–484.

[48] L. Espié, Etude expérimentale et modélisation numérique du comportement de monocristaux de superalliages, PhD Thesis, École Nationale Supérieure des Mines de Paris (1996).

[49] A. Fredholm, Monocristaux d'alliages base nickel relation entre composition, microstructure et comportement en fluage à haute température, Ph.D. thesis, École Nationale Supérieure des Mines de Paris (1987).

[50] D. Ayrault, Fluage à haute température de superalliages base nickel monocristallins, Ph.D. thesis, École Nationale Supérieure des Mines de Paris (1989).

[51] A.G. Khachaturyan, S. Semenovskaya, T. Tsakalakos, Elastic strain energy of inhomogeneous solids, Phys. Rev. B 52 (1995) 15909–15919.

[52] R. Desmorat and R. Marull, Non-quadratic Kelvin modes based plasticity criteria for anisotropic materials, Int. J. Plasticity 27 (2011) 328–351.